

NUSTAR HARD X-RAY OBSERVATIONS OF THE ENERGETIC MILLISECOND PULSARS PSR B1821–24, PSR B1937+21, AND PSR J0218+4232

E. V. GOTTHELF¹ AND S. BOGDANOV

Columbia Astrophysics Laboratory, Columbia University, 550 West 120th Street, New York, NY 10027, USA

Draft version October 11, 2018

ABSTRACT

We present *Nuclear Spectroscopic Telescope Array* (*NuSTAR*) hard X-ray timing and spectroscopy of the three exceptionally energetic rotation-powered millisecond pulsars PSRs B1821–24, B1937+21, and J0218+4232. By correcting for frequency and phase drifts of the *NuSTAR* onboard clock, we are able to recover the intrinsic hard X-ray pulse profiles of all three pulsars with a resolution down to $\leq 15 \mu\text{s}$. The substantial reduction of background emission relative to previous broadband X-ray observations allows us to detect for the first time pulsed emission up to ~ 50 keV, ~ 20 keV, and ~ 25 keV, for the three pulsars, respectively. We conduct phase-resolved spectroscopy in the 0.5–79 keV range for all three objects, obtaining the best measurements yet of the broadband spectral shape and high-energy pulsed emission to date. We find extensions of the same power-law continua seen at lower energies, with no conclusive evidence for a spectral turnover or break. Extrapolation of the X-ray power-law spectrum to higher energies reveals that a turnover in the 100 keV to 100 MeV range is required to accommodate the high-energy γ -ray emission observed with *Fermi*-LAT, similar to the spectral energy distribution observed for the Crab pulsar.

Subject headings: pulsars: general — pulsars: individual (PSR B1821–24, PSR B1937+21, PSR J0218+4232) — stars: neutron — X-rays: stars

1. INTRODUCTION

Millisecond pulsars (MSPs) represent a distinct population of old rotation-powered pulsars with short spin periods, $P \leq 25$ ms, and small spin-down rates, typically of order $\dot{P}_i \sim 10^{-20}$. Their timing properties imply a relatively low surface magnetic dipole field strength of $B_{\text{surf}} \propto (P\dot{P}_i)^{1/2} \sim 10^8 - 10^{10}$ G and a large characteristic spin-down age of $\tau \equiv P/2\dot{P}_i \geq 1$ Gyr. These rapidly rotating neutron stars (NSs) are spun up by accretion of matter and angular momentum from a close stellar companion in a low-mass X-ray binary.

Of the ~ 300 known radio MSPs, dozens have been detected in X-rays, and are broadly grouped into three distinct categories based on their dominant emission mechanism: (i) pulsed thermal radiation from the NS magnetic polar caps (e.g., Bogdanov et al. 2006; Zavlin 2006; Forestell et al. 2014), (ii) unpulsed shock emission due to a pulsar wind-driven intrabinary shock (e.g., Bogdanov et al. 2005, 2014), and (iii) pulsed non-thermal radiation from the pulsar magnetosphere (see, e.g., Zavlin 2007, and references therein).

The MSPs in the latter category provide an important testbed for theoretical models of pulsar electrodynamics and emission physics because they exhibit remarkably similar properties to non-recycled young pulsars like the Crab, this despite their faster spin (and as a result, much lower altitude of the pulsar light cylinder) and weaker surface magnetic fields ($\sim 10^8 - 10^9$ G). This is likely a consequence of their high magnetic fields in the vicinity of the light cylinder ($\sim 10^5$ G), where the non-thermal radiation is thought to originate. These MSPs are also Crab-like in the sense that they are known to exhibit gi-

ant radio pulses (Cognard et al. 1996; Romani et al. 2001; Knight et al. 2006), which in the case of PSR J0218+4232 appear to be closely aligned in spin phase with the two soft X-ray pulses. Constraining the X-ray emission properties over as wide a photon energy range as possible may offer vital clues regarding the emission physics of MSPs, and by extension, all pulsars. Specifically, important insight into the detailed physics of MSP magnetospheric emission can be gained by investigating the energy dependence of the pulsations and the broadband high-energy (soft X-rays through γ -rays) spectral properties of these pulsars.

In this paper, we present the first *Nuclear Spectroscopic Telescope Array* (*NuSTAR*) hard X-ray (3–79 keV) observations of three magnetospherically driven MSPs, PSRs B1821–24, B1937+21, and J0218+4232, whose properties are given in Table 1. These are among the most energetic MSPs known and the only ones in their category sufficiently bright to measure above 10 keV. The *NuSTAR* data allow us to study their X-ray spectra in an energy range beyond what was previously possible and to consider their broader spectral energy distribution (SED) with respect to *Fermi* Large Area Telescope (LAT) spectra. To fully exploit the phase information for these rapidly spinning pulsars (1.6–3.0 ms) we devise a method to self-correct the data for drift and fluctuations of the *NuSTAR* clock, whose short-term timing variance is otherwise on the order of the pulse periods for all three pulsars.

This work is laid out as follows. In §2, we present our *NuSTAR* observation of PSR B1821–24, along with a spectroscopic reanalysis of archival *RXTE* and *Chandra* data. These observations and their reductions are detailed in §2.1. In §2.2 we explain our technique used to correct the photon arrival time for *NuSTAR* clock inaccuracies. The resulting timing, image, and spec-

¹ Departament de Física Quàntica i Astrofísica, Institut de Ciències del Cosmos, Universitat de Barcelona, IEEC-UB, Martí i Franquès 1, E-08028, Barcelona, Spain

TABLE 1
SUMMARY OF THE PROPERTIES OF MSPs¹ OBSERVED WITH *NuSTAR*

Pulsar (PSR name)	R.A. (J2000)	Decl. (J2000)	d (kpc)	P (ms)	\dot{P}	\dot{E} (erg s ⁻¹)	B (G)	Type
J0218+4232	02 18 06.3	+42 32 17.3	3.15	2.323	7.74×10^{-20}	2.44×10^{35}	4.29×10^8	Magnetospheric
J0437-4715	04 37 15.8	-47 15 09.1	0.16	5.757	5.73×10^{-20}	1.19×10^{34}	5.81×10^8	Thermal
J1023+0038	10 23 47.6	+00 38 40.8	1.37	1.688	1.20×10^{-20}	9.85×10^{34}	1.44×10^8	intrabinary shock
J1227-4853	12 27 58.7	-48 53 42.7	1.80	1.686	1.11×10^{-20}	9.13×10^{34}	1.38×10^8	intrabinary shock
J1723-2837	17 23 23.1	-28 37 57.1	0.72	1.856	7.54×10^{-21}	4.66×10^{34}	1.20×10^8	intrabinary shock
B1821-24	18 24 32.0	-24 52 10.8	5.50	3.054	1.62×10^{-18}	2.24×10^{36}	2.25×10^9	Magnetospheric
B1937+21	19 39 38.5	+21 34 59.1	3.50	1.558	1.05×10^{-19}	1.10×10^{36}	4.09×10^8	Magnetospheric
J2129-0429	21 29 45.0	-04 29 05.5	1.10	7.620	2.60×10^{-19}	3.90×10^{34}	1.42×10^9	intrabinary shock
J2339-0533	23 39 38.7	-05 33 05.3	1.10	2.884	1.41×10^{-20}	2.32×10^{34}	2.04×10^8	intrabinary shock

Note. Compiled from the ATNF radio pulsar catalog (Manchester et al. 2005). Provenance of coordinates used for the barycenter corrections is given in the text. The *NuSTAR* observations of the center of 47 Tuc, which contains at least 25 MSPs (Pan et al. 2016), are not included in this Table; X-ray emission from the MSPs in 47 Tuc is completely dominated by the bright overlapping LMXB X9 (Bahramian et al. 2017) and are not detectable.

tral analyses for PSR B1821-24 is presented in §2.3-2.5, respectively. In §3, we present spectral analysis of archival *NuSTAR*, *Chandra*, and *XMM-Newton* data for PSR B1937+21; the results are given in §3.1. Similarly, in §4 we present the observations and results of a spectroscopic analysis of PSR J0218+4232 using existing *NuSTAR* and *XMM-Newton* data. In §5, we discuss the SED of the three MSPs and offer conclusions in §6.

2. PSR B1821-24

The bright 3.05 ms pulsar PSR B1821-24 (also known as PSR J1824-2452A) resides in the globular cluster M28 and has the distinction of being the most energetic MSP known, with a spin-down luminosity² of $\dot{E} = 2.2 \times 10^{36}$ ergs s⁻¹. It was the first MSP discovered in a globular cluster (Lyne et al. 1987) and the first from which non-thermal pulsed X-rays were detected (using *ASCA*; Saito et al. 1997). Nearly all of the X-ray emission from PSR B1821-24 is contained within two exceptionally narrow pulse peaks, with a duty cycle of only a few percent (Rutledge et al. 2004; Ray et al. 2008).

The non-thermal spectrum of PSR B1821-24 is well-characterized by an absorbed power-law model with photon index $\Gamma \approx 1.3$ yielding a luminosity of $L(0.3-8 \text{ keV}; 5.5 \text{ kpc}) = 1.4 \times 10^{33} \Theta \text{ erg s}^{-1}$, where Θ is an unknown beaming fraction of the X-ray emission pattern (Rots et al. 1998; Bogdanov et al. 2011). In this sense, PSR B1821-24 is more similar to the young, energetic pulsars than to a typical MSP. Measurements with *RXTE*, sensitive in the hard X-ray band (2-100 keV), are only able to detect pulsations up to ~ 13 keV, despite deep observations (see, e.g., Rots et al. 1998; Ray et al. 2008). Whether this is an intrinsic cutoff on the pulsar flux or an instrumental limitation is unknown.

In the following subsections, we present *NuSTAR* observations of PSR B1821-24, analyzed together with the accumulated *Chandra* and *RXTE* data, which allows us to extend the previous spectral results up to 79 keV.

2.1. OBSERVATIONS AND ANALYSIS

² The measured spin-down rate \dot{P} and derived spin-down luminosity $\dot{E} \propto \dot{P}/P^3$ are not significantly affected by the acceleration of the pulsar in the globular cluster potential (see Johnson et al. 2013).

2.1.1. *NuSTAR*

We observed PSR B1821-24 with *NuSTAR* on 2015 June 6 (ObsId 30101053002) and on 2015 June 21 (ObsId 30101053004), as part of the AO1 Guest Observer program. *NuSTAR* consists of two co-aligned X-ray telescopes, with the corresponding focal plane modules FPMA and FPMB that provide 18'' FWHM imaging resolution over a 3-79 keV X-ray band with a characteristic spectral resolution of 400 eV FWHM at 10 keV (Harrison et al. 2013). The reconstructed *NuSTAR* coordinates are accurate to 7''5 at the 90% confidence level. The nominal timing accuracy of *NuSTAR* is ~ 2 ms rms, after correcting for drift of the onboard clock, with the absolute timescale shown to be better than < 3 ms (Mori et al. 2014; Madsen et al. 2015). Although this is insufficient to resolve the 3.05 ms period of PSR B1821-24, we devise a method, presented herein, to correct the photon arrival times to better than 15 μ s accuracy.

NuSTAR data were reprocessed and analyzed using FTOOLS 09May2016_V6.19 (NUSTARDAS 14Apr16_V1.6.0) with the *NuSTAR* Calibration Database (CALDB) files of 2016 July 6. The resulting data set provides a total of 140.7 ks and 55 ks of net good exposure time for the two pointings, respectively. For the timing analysis, the nominal *NuSTAR* clock correction was applied to the photon arrival times which are converted to barycentric dynamical time (TDB) using the DE405 solar system ephemeris and radio timing coordinates of Ray et al. (2008). For all subsequent analysis we merged data from both FPM detectors.

Although the globular cluster M28 hosts at least 11 other pulsars (Bégin 2006), they are all over a factor of ~ 100 fainter than PSR B1821-24 in X-rays (Bogdanov et al. 2011) and thus cannot be studied effectively with *NuSTAR*.

2.1.2. *RXTE*

PSR B1821-24 has been observed extensively in hard X-rays with *RXTE* during the mission lifetime, primarily for the purpose of absolute spacecraft time calibration and to measure the X-ray-to-radio phase lags (Rots et al. 1998; Ray et al. 2008). In anticipation of the *NuSTAR* observations, we collectively analyzed all available archived *RXTE* data on PSR B1821-24 for the first time.

A total of 180 ks of exposure times were accumulated during three programs: P20159 (1997 Feb 12-13, 16.9 ks), P90053 (2005 Feb 28-Mar 1, 14.9 ks), P92008 (2006 Jul 6-8, 48.4 ks ; 2006 Oct 9-10, 51.2 ks ; 2007 Apr 25-26, 48.5 ks). These observations were made with the Proportional Counter Array (PCA; Jahoda et al. 1996) onboard *RXTE*. The PCA consists of five collimated xenon proportional counter units (PCUs), each having a front propane anticoincidence layer, with a total effective area of $\sim 6500 \text{ cm}^{-2}$ over a 1° field of view (FWHM). Each PCU is sensitive to photons in the energy range of 2 – 60 keV, with an energy resolution of 18% at 6 keV recorded in 256 channels.

Data were collected in *GoodXenonwithPropane* mode with two to five PCU modules in use at any given time, with an average of 3.7 PCUs active overall. In this mode, photon arrival times are recorded with $1 \mu\text{s}$ resolution. We analyzed events from the top xenon layers of each PCU only. Including the second layers resulted in no significant improvement in the signal-to-noise ratio. The data were time-filtered using standard criteria and analyzed using the *RXTE* FTOOLS package.

RXTE PCA phase-resolved light curves and spectra for PSR B1821–24 were constructed using *fasebin* and related FTOOLS. By folding on the radio ephemeris of Ray et al. (2008) we obtained a summed spectrum in 100 phase bins including data from the 22 observation segments. Energy-selected light curves were generated using *fbssum* and a combined spectrum comprising data from all *RXTE* programs were added using *fbadd*. Appropriate response matrices were created for each PCU using *pcarsp* for the phased-average spectra extracted using *seextrct*.

2.1.3. *Chandra*

In our analysis, we also make use of archival *Chandra* ACIS-S imaging and spectroscopic data of M28 from 2002 (ObsIDs 2684, 2685, 2683) and 2008 (ObsIds 9132, 9133) totaling 240 ks and previously presented in Becker et al. (2003), Bogdanov et al. (2011), and Servillat et al. (2012). We also consider *Chandra* HRC-S observations of PSR B1821–24 obtained in timing mode (ObsIDs 2797 and 6769), which offer $16 \mu\text{s}$ time resolution. The HRC is most sensitive to photons below 2 keV but provides no useful spectral information. The data reduction and analysis procedures of all *Chandra* observations are detailed in Bogdanov et al. (2011).

2.2. Correcting the *NuSTAR* Photon Arrival Times

Before we can take advantage of the millisecond time resolution available with the *NuSTAR* FPM imagers we must address several clock issues relevant to observing MSPs. The *NuSTAR* clock frequency is known to drift at a steady rate over time and is typically adjusted every few days by means of a coarse divisor to limit the wandering from a nominal 24 MHz rate. A model of the clock drift is stored in the clock-correction file and used by the FTOOL *barycorr* to correct the *NuSTAR* photon arrival times in conjunction with the barycenter correction. However, unaccounted-for root mean square residuals of order $\sim 2 \text{ ms}$ remain in the clock drift model.

In addition, during telemetry downlinks (several times a day) the spacecraft times are adjusted to the coordinated universal time (UTC) system. This can intro-

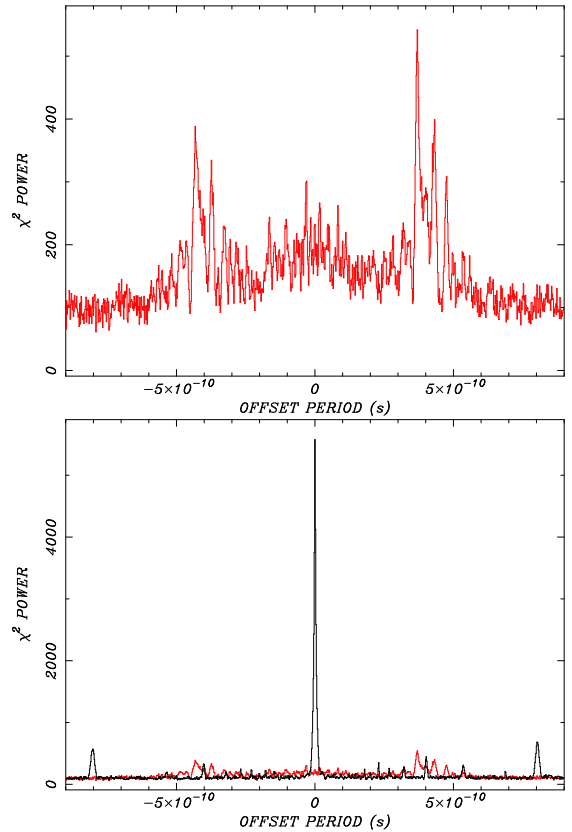


FIG. 1.— *NuSTAR* periodogram of PSR B1821–24 folded around the expected 3.05 ms spin period. Top: result obtained for the nominal processed data set. Power in the pulsed signal is spread out over a number of “sidebands” around the expected period. Bottom: the result obtained using the same data set corrected for timing inaccuracies, as described in §2.2 (black). The periodogram of the uncorrected data (red) from the upper panel is reproduced for reference.

duce a phase shift due to an uncalibrated $\sim 1 \text{ ms}$ relative offset in the absolute time stamps between ground stations (C. Markwardt, private communication). To circumvent the latter potential problem, all data for the PSR B1821–24 observations were acquired using a single (Malindi) ground station, as was used for the other two pulsars discussed herein. A complete description of the *NuSTAR* event time assignment can be found in Madsen et al. (2015).

Most consequential for fast pulsar timing is the variability of the clock rate on orbital timescales (97 minutes). Our investigation of the *NuSTAR* timing data reveals that the clock is stable to better than at least $15 \mu\text{s}$ during the spacecraft night, when the solar illumination of the spacecraft is Earth-blocked. However, during spacecraft day, the clock evidently wanders sufficiently between orbit-to-orbit observing intervals to lose phase cycle count for a millisecond pulsar. Thus, it is not possible to recover a coherently pulsed signal over several orbits. This is best illustrated by a pulsar search for PSR B1821–24 around the expected frequency using the nominal *NuSTAR* processing, including barycenter and clock corrections. As shown in the top panel of Figure 1, the search periodogram yields a complex power spectrum of low significance with a multitude of “sidebands” spanning $\delta f \approx 9 \times 10^{-5} \text{ Hz}$.

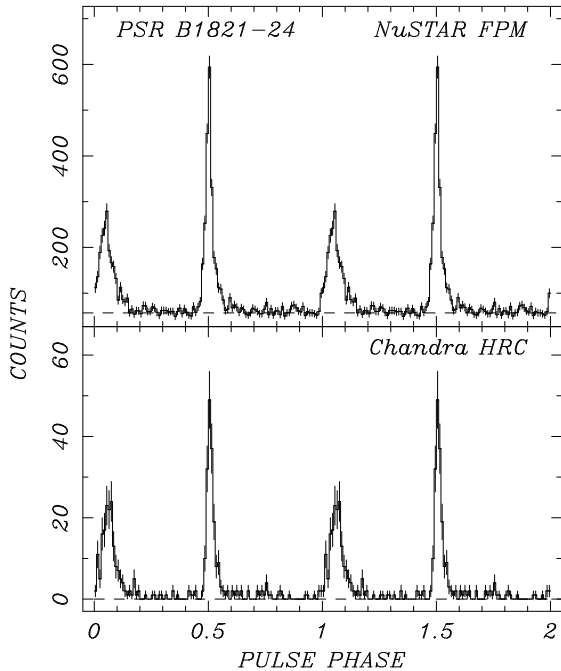


FIG. 2.— Comparison of the *NuSTAR* (Top) and *Chandra* (Bottom) pulse profiles of the 3.05 ms pulsar PSR B1821–24. The *NuSTAR* 3–79 keV data are corrected for timing inaccuracies, as described in §2.2 and the *Chandra* HRC data were obtained in timing mode. The two data sets complement each other, with the HRC data dominant below 2 keV and the *NuSTAR* data above 3 keV. The background level is indicated by the dashed line. The profiles contain 100 phase bins and phase zero is arbitrarily aligned so that the main pulse peak falls on $\phi = 0.5$. Two cycles are shown for clarity.

Fortunately, the observations of PSR B1821–24 were taken exclusively during intervals of Earth-block and its pulsed signal is sufficiently strong to measure a pulse frequency and phase over a single orbit. For the 60 orbits that constitute the full data set, on average 75 photons per orbit were collected in the source aperture for a typical 3.3 ks of exposure. Detecting a signal with such few photons is uniquely possible because of the very sharp, asymmetric double peak profile, with $\approx 100\%$ modulation and very low detector background. We use this fact to correct errors in the frequency and phase introduced between orbits.

Our method is to break up the observation into orbit-sized segments and correct for the advanced or retarded clock rate by adjusting the photon arrival times in the following sense,

$$t' = t \times \alpha_i + \beta_i$$

where, for the i th segment, α_i is the ratio of the observed frequency of the pulsar relative to the expected frequency, and β_i is the phase offset at the adjusted times relative to the expected phase. The scale factors α_i , around $\pm 4 \times 10^{-8}$, are measured using the χ^2 statistic, optimal for the complex pulse shape. The phase offsets β_i are determined by cross-correlating the pulse profile for each segment with an iterated high-statistic template. The β_i 's ensure that the scaled photon arrival times for each orbit align on the fiducial ephemeris relative to the start of the observation, with the main peak (P1) ad-

justed to phase $\phi_{P1} = 0.5$. This method accounts for all unmodeled orbit-to-orbit clock shifts.

To construct the set of 60 α 's and β 's for PSR B1821–24, we extracted photons from an optimal combination of source aperture ($r = 0.85'$) and energy range (3–25 keV) that maximizes the pulsar signal and cross-correlated the folded light curves for each segment in 100 phase bins with the template. We applied these coefficients to the photon arrival times to generate the corrected event files that can now be coherently folded on the input ephemeris to recover the full pulsar signal.³ These files are used in all subsequent phase-resolved imaging and spectral analysis presented below. The resulting periodogram search using the corrected data is shown in the bottom panel of Figure 1.

2.3. *NuSTAR* Timing Analysis

The folded light curve, using data merged from both *NuSTAR* pointings of PSR B1821–24, fully resolves the peak of the pulsed signal in 30 μ s phase bins, limited ultimately by the accuracy of the cross-correlations, detailed above. In Figure 2, we compare the 3–79 keV *NuSTAR* pulse profile to the *Chandra* HRC profile, obtained from a 3" diameter aperture, barycentered and folded on the ephemeris of Ray et al. (2008). Although the HRC is most sensitive to photons below 2 keV, there is no clear energy dependence; the observed morphology of the two profiles are very similar, showing the same sharp, asymmetric peak, despite the non-overlapping energy bands. The background level, estimated from a circular annulus accounts for nearly all of the off-pulse flux. A small contribution from the unresolved M28 X-ray sources in the *NuSTAR* point-spread function (PSF) accounts for the rest, as discussed below.

Figure 3 also compares the *NuSTAR* and *RXTE* pulse profiles in two adjacent energy bands, 3–15 and 15–79 keV. At the lower energy, the profiles from the two missions are again strikingly similar. However, above 15 keV the signal in the *RXTE* data is barely visible above the background, while the *NuSTAR* pulsations are clearly detected with high signal-to-noise ratio, up to ~ 30 keV. This pulse signal is evidently not cut off below 15 keV, but it is instead lost in the high background of the non-imaging *RXTE*. These light curves illustrate that the timing accuracy of the corrected *NuSTAR* data set can be on par with the highest quality *RXTE* and *Chandra* data.

2.4. *NuSTAR* Image Analysis

PSR B1821–24 is situated in the dense core of M28 where numerous other X-ray sources are present, as seen in the sub-arcsecond angular resolution *Chandra* images (Becker et al. 2003; Bogdanov et al. 2011). To the *NuSTAR* imaging resolution, the M28 cluster core is unresolved. This does not pose a problem since PSR B1821–24 is the brightest source above ~ 5 keV. Indeed, the bright hard X-ray source in M28 has a position fully consistent with that of PSR B1821–24. The transient IGR J1824–24525 in M28 occasionally reaches

³ However, we cannot be sure that the phase count was strictly maintained. For example, if the phase count were lost, it may not be possible to fold coherently a second pulsar in the field using the corrections for PSR B1821–24.

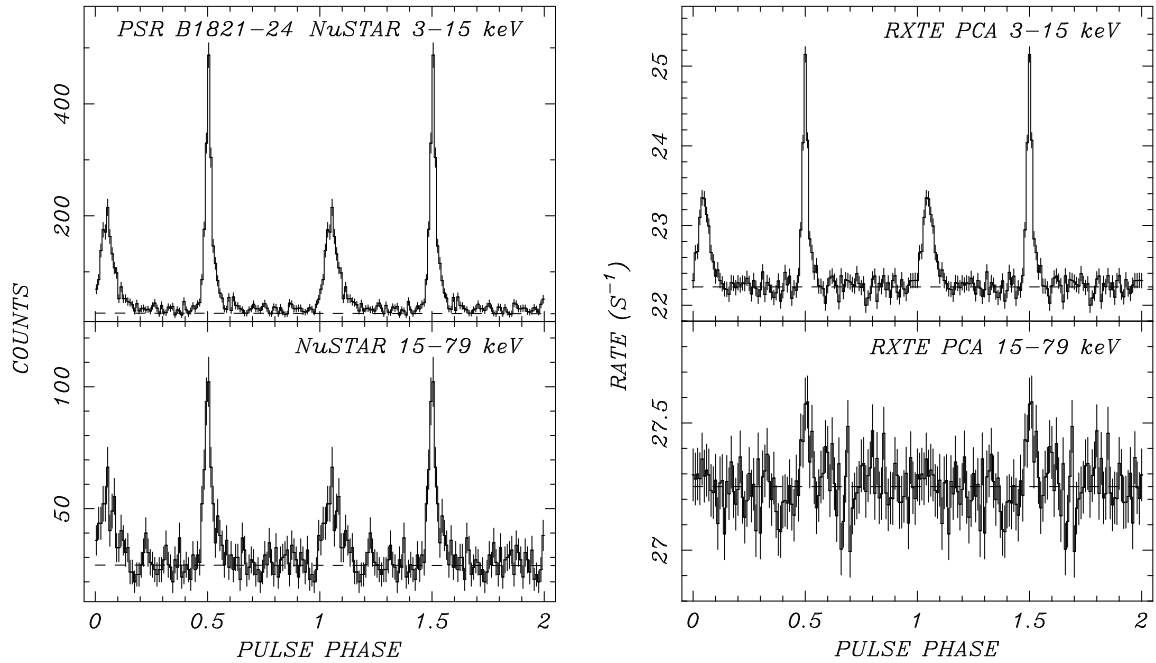


FIG. 3.— Comparison of the *NuSTAR* (left) and *RXTE* (right) pulse profiles of PSR B1821–24 in two energy bands. The *NuSTAR* photon arrival times have been corrected for timing inaccuracies, as described in §2.2, and the *RXTE* PCA data are from the top layer only. The background level is indicated by the dashed line. These profiles contain 100 phase bins and phase zero is arbitrarily aligned so that the main pulse peak falls on $\phi = 0.5$. Two rotational cycles are shown for clarity.

comparable or higher luminosities and exhibits a hard spectrum (Papitto et al. 2013; Linares et al. 2014). However, this object spends the vast majority of the time in a dormant state, with luminosity $\sim 10^{31}$ erg s $^{-1}$ so its quiescent emission in the hard X-ray band during the *NuSTAR* exposure is negligible for all practical purposes.

Figure 4 presents 3–20 keV exposure-corrected images of the *NuSTAR* M28 field smoothed using a $\sigma = 3''.7$ Gaussian kernel and scaled linearly. To look for possible unpulsed X-ray emission from PSR B1821–24 we examined the *NuSTAR* phase-average, on-pulse, and off-pulse images. We define the phase range corresponding to the on-pulse interval to include photons from both pulse peaks, P1 (10 of 100 phase bins) and P2 (16 of 100 phase bins), with the off-pulse interval containing the remaining phase bins (see Figure 2).

The phase-averaged *NuSTAR* image shows the bright pulsar as well as the emission coincident with *Chandra* source #4 reported by Becker et al. (2003), likely an active galactic nucleus or a cataclysmic variable, to the northwest of PSR B1821–24. Also evident in the image is a large bright crescent of emission that corresponds to contamination from single-bounce photons off the *NuSTAR* optics originating from the bright X-ray binary GS 1826–24 (Ubertini et al. 1999), which is situated 1.6° from the core of M28. From the off-pulse image it is clear that there is detectable emission at the location of the pulsar after accounting for the off-source background. This remainder can be attributed to hard X-ray emission from the numerous other sources in M28 that are unresolved by *NuSTAR*. We estimate this component from the scaled *Chandra* flux in the 3–10 keV band that fall within the *NuSTAR* PSF. Its contribution is fully consistent with the off-pulse component of the light curve in the same band, after allowing for the local *NuSTAR* back-

ground. Also evident in the off-pulse image is an object just to the southwest of the pulsar consistent with the position of *Chandra* source #17 identified by Becker et al. (2003), which is a candidate cataclysmic variable. The final panel of Figure 4 presents the off-pulse-subtracted phase-averaged image, providing a clean representation of the *NuSTAR* PSF of the pulsar, as expected.

2.5. X-Ray Spectroscopy

In all of the following spectral analyses, extracted spectra, grouped into appropriate channels, were fitted to an absorbed power-law spectrum model using the XSPEC (v12.8.2) package (Arnaud 1996). All spectral fits use the TBabs absorption model in XSPEC with the wilm solar abundances (Wilms et al. 2000) and the vern photoionization cross-section (Verner et al. 1996).

2.5.1. RXTE and Chandra Spectroscopy

To isolate the purely pulsed emission for the *RXTE* data, we used the scaled off-pulse phase intervals for a background spectrum. This provides a perfect representation of the non-pulsed emission. The resulting background-subtracted *RXTE* spectrum of PSR B1821–24 is then fit simultaneously with the 240 ks *Chandra* ACIS-S3 (spatially isolated but phase-averaged) pulsar spectrum presented in Bogdanov et al. (2011), with their normalizations unlinked.

The available *RXTE* data contain no useful spectral information above ~ 13 keV. This is not necessarily due to the background, which exceeds the source rate by an order of magnitude at all energies, but rather for the lack of source photons and the large uncertainty in subtracting two comparably large numbers. With the column density fixed to the *Chandra*-derived value of $N_H = 2.4 \times 10^{21}$ cm $^{-2}$ (Bogdanov et al. 2011), the best-

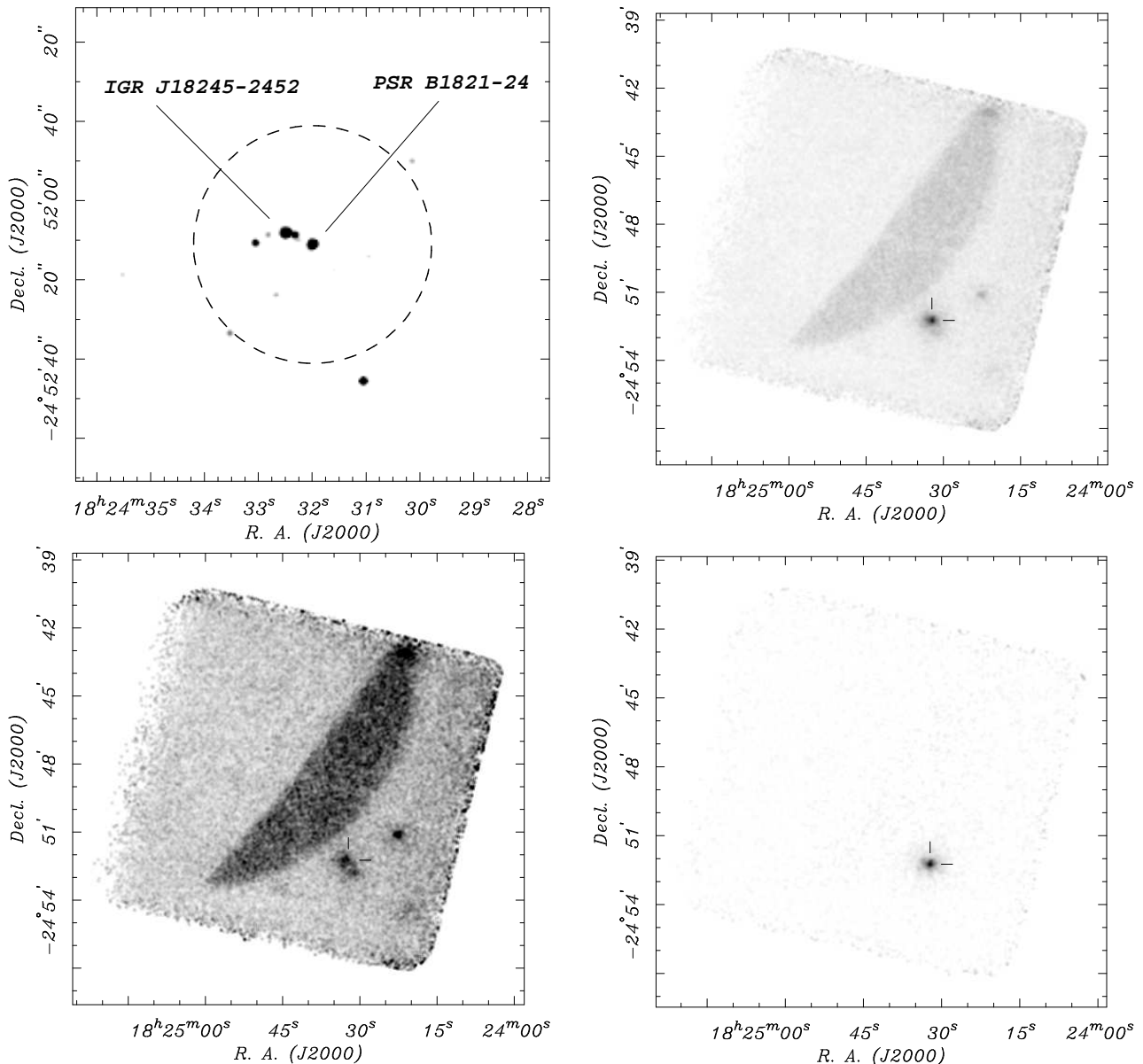


FIG. 4.— Top left — A reference high-resolution *Chandra* ACIS-S 3–10 keV image of the core of M28. The dashed circle of radius 0.5' centered on PSR B1821–24 corresponds to the $\sim 50\%$ enclosed fraction of the *NuSTAR* point-spread function. In this observation from 2008, the transient source IGR J18245–2452 (Papitto et al. 2013) was more luminous than PSR B1821–24 but was ~ 2 orders of magnitude fainter at the time of the *NuSTAR* observations in 2015. Above ~ 3 keV, PSR B1821–24 is by far the brightest persistent source in M28. Other three panels — *NuSTAR* exposure-corrected and smoothed 3–20 keV X-ray images of the field containing PSR B1821–24. *Top right* — The pulse phase-averaged image showing the pulsar and source #4 from Becker et al. (2003). Also evident is stray light contamination from the luminous X-ray binary GS 1826–24. *Bottom left* — The off-pulsar image that shows evidence of contamination from unresolved hard sources in M28 coincident with PSR B1821–24. *Bottom right* — The pulsar image generated by subtracting the scaled off-pulse image from the phase-averaged image.

fit ($\chi^2 = 0.88$ for 198 d.o.f.), power-law model in the < 15 keV band yields a photon index of $\Gamma = 1.25^{+0.12}_{-0.14}$, in agreement with *Chandra* results at lower energies. There is no evidence for flux variability. This result represents the best X-ray spectroscopy available for PSR B1821–24 prior to the *NuSTAR* result presented below.

2.5.2. *NuSTAR* Spectroscopy

We can improve on the *RXTE* result by taking advantage of the greatly decreased *NuSTAR* background to extend the spectral measurements up to 79 keV. As with the *RXTE* phase-resolved spectroscopy analysis, we

isolate the *NuSTAR* spectrum of the pulsar into two pulse peaks and define a clean representation of the background using the scaled off-pulsed spectrum. Spectra were produced using the `nuproducts` script in the *NuSTAR* FTOOL package acting on the phase-resolved data files. The spectra are fitted using instrument and mirror response files generated for the phase-averaged spectra. We add the spectra derived from the two detectors and two observations to produce our final phase-averaged, on-pulse, and off-pulse spectral and weighted response files.

The *Chandra* and *NuSTAR* spectra were both binned with a minimum of 30 counts per channel and fitted si-

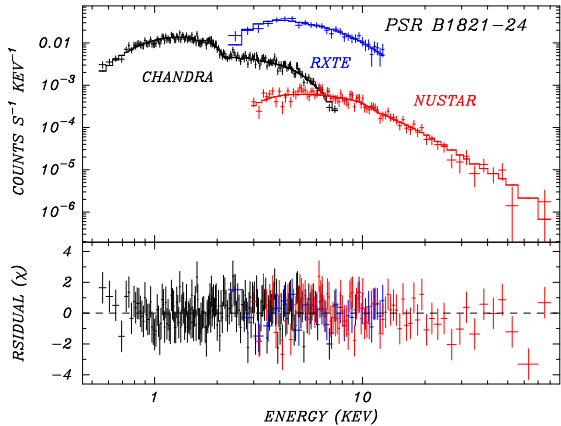


FIG. 5.— Phase-resolved *NuSTAR* and *RXTE* spectra of PSR B1821–24 fitted simultaneously with the phase-averaged *Chandra* spectrum to an absorbed power-law model with independent normalizations. The upper panel presents the *Chandra* (black), *RXTE* (blue), and *NuSTAR* (red) spectral data points (crosses) along with the best-fit model (solid lines) given in Table 2. The lower panel shows the fit residuals in units of sigma.

multaneously with the *RXTE* data to an absorbed power-law model with independent normalizations. The three data sets were restricted to the 0.5–8 keV, 3–50 keV, and 2–13 keV energy bands, respectively. The resulting fit yields a column density of $(4.0 \pm 0.4) \times 10^{21} \text{ cm}^{-2}$ and a photon index of $\Gamma = 1.28 \pm 0.05$ with $\chi^2_\nu = 0.91$ for 226 degrees of freedom and an absorbed *NuSTAR* flux in the 2–10 keV band of $(3.7 \pm 0.2) \times 10^{-13} \text{ erg cm}^{-2} \text{ s}^{-1}$ and $(3.8 \pm 0.1) \times 10^{-13} \text{ erg cm}^{-2} \text{ s}^{-1}$ for the *Chandra* spectrum (see Figure 5). All quoted uncertainties are at a 90% confidence level (C.L.). For a distance to M28 of 5.5 kpc (Servillat et al. 2012), the derived fluxes imply an X-ray luminosity of $4 \times 10^{33} \Theta \text{ erg s}^{-1}$ in the 0.3–79 keV range. There is no requirement for an additional thermal component such as may arise due to heated polar caps. The relative *Chandra* and *NuSTAR* fluxes are in agreement at the 90% confidence level (C.L.). A summary of the spectral results is given in Table 2.

As noted in Bogdanov et al. (2011), there may be pileup distortions of the *Chandra* spectrum at a level of a few percent, which can artificially harden the intrinsic source spectrum. Applying a pileup component to the model for the *Chandra* data results in $\Gamma = 1.29 \pm 0.07$ for the joint fit, in excellent agreement with the joint fit without pileup. This is an indication that event pile-up in the *Chandra* data do not significantly bias the results. Fitting the *NuSTAR* data alone with the column density fixed to the above value yields a marginally steeper photon index of $\Gamma = 1.36 \pm 0.07$, suggesting the possibility of curvature in the spectrum, as seen in the pulsed Crab spectrum.

We also examined the *NuSTAR* spectra from the individual pulses, P1 and P2, and find no significant difference in their photon indices, $\Gamma_{P1} = 1.36 \pm 0.09$ versus $\Gamma_{P2} = 1.33 \pm 0.11$, in agreement to within 2%, well within their uncertainties. The unabsorbed flux ratio for the two pulses is found to be $F_{P1}/F_{P2} = 1.26$.

3. PSR B1937+21

PSR B1937+21 (also referred to as PSR J1939+2134) was the first MSP discovered (Backer et al. 1982) and

for 25 years the fastest spinning pulsar known ($P = 1.55$ ms). With a spin-down luminosity of $\dot{E} = 1.1 \times 10^{36} \text{ ergs s}^{-1}$, it is the second most energetic MSP detected. This isolated pulsar lies in the Galactic plane at a distance of ~ 3.5 kpc. At X-ray energies, PSR B1937+21 has been detected as a pulsed source with *ASCA* (Takahashi et al. 2001), *BeppoSAX* (Nicastro et al. 2004), *RXTE* (Guillemot et al. 2012), *Chandra* and *XMM-Newton* (Ng et al. 2014). In hard X-rays, the pulsar has so far only been detected up to ≈ 13 keV with *RXTE* (Guillemot et al. 2012). Like PSR B1821–24, this MSP shows sharp pulsations with a small duty cycle and nearly 100% pulsed fraction.

3.1. Observations and Results

We examined the 41 ks *NuSTAR* observation of PSR B1937+21 obtained on 2015 Aug 29 as part of the Cycle 1 Guest Observer program (ObsID 30101031002; PI Ng). These data were extracted, reduced, and analyzed in the same fashion as described above for PSR B1821–24. For the timing correction, an average of 66 counts per orbit were collected during 14 segments. The pulse signal from PSR B1937+21 detected in a segment is sufficiently strong to allow us to reproduce the method presented in §2.2 to correct the photon arrival times. We used the most current published pulsar ephemeris (Desvignes et al. 2016) to barycenter and phase align the pulse profile over the course of the *NuSTAR* observation.

PSR B1937+21 was also observed with *XMM-Newton* on 2010 March 29 for a total exposure of 66.9 ks (ObsID 0605370101). These data were originally presented in Ng et al. (2014). The EPIC pn data for this observation were collected in timing mode, which offers 30 μs time resolution but imaging along one dimension only. This data is not used here for spectroscopy due to known spectral issues for this mode.

The folded light curves from the two missions are shown in Figure 6. It is clear that the *NuSTAR* pulse profile is fully resolved and is comparable to the best *XMM-Newton* timing mode observations, also shown in Ng et al. (2014). The hard X-ray pulse profile for PSR B1937+21 is qualitatively similar to that of PSR B1821–24, but with a much suppressed secondary peak. The profile of the main peak displays the same characteristic asymmetry clearly evident in PSR B1821–24 and is detectable up to ~ 25 keV with *NuSTAR*, while the faint secondary pulse is lost to the background above ~ 8 keV. Given that the *NuSTAR* off-pulse emission is fully consistent with the estimated background, we conclude that the timing signal from PSR B1937+21 is 100% pulsed.

For the spectroscopic analysis of PSR B1937+21, we combined *NuSTAR*, *XMM-Newton* and *Chandra* data. Following the recipe described previously, we extracted a *NuSTAR* on-pulse spectrum of PSR B1937+21 and the off-pulse spectrum to use as background. We extracted the *XMM-Newton* spectrum from the EPIC MOS1/2 data following the standard procedures as outlined in Ng et al. (2014). We also retrieved an archival 49.5 ks *Chandra* ACIS-S observation obtained on 2005 June 26 (ObsID 5516), which we processed and reduced as detailed in Ng et al. (2014). We used phase-averaged *XMM-Newton* and *Chandra* spectra as the time resolution of these data sets does not allow a phase-resolved spectral analysis.

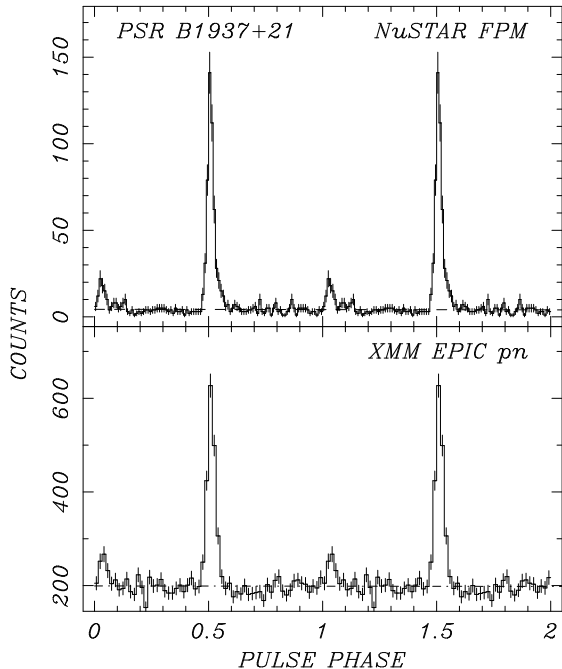


FIG. 6.— Comparison of the *NuSTAR* (top) and *XMM-Newton* (bottom) pulse profiles of the 1.55 ms pulsar PSR B1937+21. The *NuSTAR* 3–25 keV data are corrected for timing inaccuracies, as described in §2.2, and *XMM-Newton* EPIC-pn data were obtained in fast timing mode. The background level is indicated by dashed line. These profiles contain 100 and 60 phase bins for the *NuSTAR* and *XMM-Newton* data, respectively. Phase zero is arbitrarily aligned so that the main pulse peak falls on $\phi = 0.5$. Two cycles are shown for clarity.

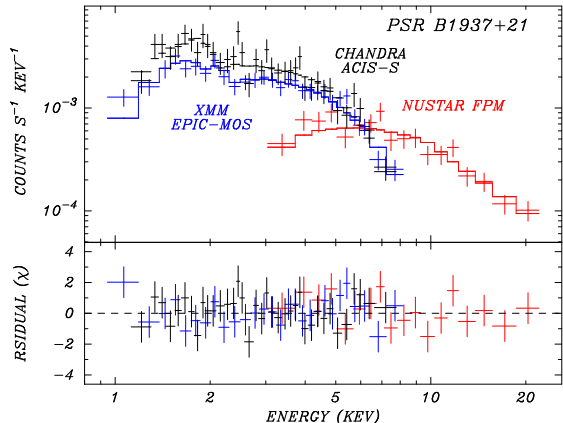


FIG. 7.— Phase-resolved *NuSTAR* spectrum of PSR B1937+21 fitted simultaneously with the phase-averaged *Chandra* and *XMM-Newton* MOS spectrum to an absorbed power-law model with independent normalizations. The upper panel presents the *Chandra* (black), *XMM-Newton* (blue), and *NuSTAR* (red) spectral data points (crosses) along with the best-fit model (solid lines) given in Table 2. The lower panel shows the fit residuals in units of sigma.

The resulting simultaneous fit to the three data sets over the 0.5–25 keV range is shown in Figure 7. Above 25 keV, the background flux dominates the *NuSTAR* spectrum. The best-fit absorbed power-law model yields an absorbing column $N_{\text{H}} = (1.78 \pm 0.27) \times 10^{22} \text{ cm}^{-2}$ and spectral index $\Gamma = 1.16 \pm 0.11$ with $\chi^2_{\nu} = 0.91$ for 83 dof. The measured *NuSTAR* 2–10 keV unabsorbed flux is $(2.37 \pm 0.29) \times 10^{-13} \text{ erg s}^{-1} \text{ cm}^{-2}$. The *XMM-Newton* flux is 10% higher, but consistent with

imperfect background subtraction and local contamination (see Ng et al. 2014). The *Chandra* unabsorbed flux, $(2.95 \pm 0.26) \times 10^{-13} \text{ erg s}^{-1} \text{ cm}^{-2}$, is also higher, by 20% at 1 keV, compared to the *NuSTAR* value, a difference significant at the 1.7σ level. This may be indicative of curvature in the spectrum.

4. PSR J0218+4232

PSR J0218+4232 is a radio luminous 2.32 ms pulsar (Navarro et al. 1995) in a two-day orbit with a helium white dwarf companion, at a distance of ≈ 3 kpc. Its spin-down properties imply $\dot{E} = 2.4 \times 10^{35} \text{ ergs s}^{-1}$, which places it among the four most energetic MSPs known. PSR J0218+4232 was the only MSP marginally detected by EGRET, making it an appealing target for X-ray observatories. Detections in the 0.1–2.4 keV band with the *ROSAT* HRI and PSPC instruments were reported by Verbunt et al. (1996) and Kuiper et al. (1998). A subsequent study by Mineo et al. (2000) resulted in measured pulsed emission in the 1–10 keV band in *BeppoSAX* observations. Follow-up investigations have also been conducted with *Chandra* (Kuiper et al. 2002) and *XMM-Newton* (Webb et al. 2004), which confirm the previous findings of two moderately sharp pulses per period with a hard non-thermal spectrum.

PSR J0218+4232 is only just bright enough to correct the photon arrival times for the clock irregularities using the method of §2.2. The pulse is not as sharp and the signal not as strong per orbit as found for our previous MSP examples. Nevertheless, we were able to successfully recover the pulse profile, but with reduced timing resolution.

4.1. Observations and Results

NuSTAR observed PSR J0218+4232 during Cycle 1 on 2015 October 28 (ObsID 30101030002; PI Ng) resulting in a 34.7 ks effective exposure. The data for this pulsar were extracted and processed in the same way as the other two pulsars. We used the binary ephemeris from Abdo et al. (2010) to further correct the barycentered photon arrival times for the binary orbit modulation before correcting for the clock drift.

We also retrieved archival *Chandra* data of PSR J0218+4232, consisting of a 72.1 ks HRC-S exposure from 2001 November 27 (ObsID 1853) first analyzed by Kuiper et al. (2002). Source photons were extracted from a $3''$ diameter aperture and barycentered using the same radio ephemeris as used for the *NuSTAR* data.

The available archival *XMM-Newton* data of PSR J0218+4232 are from a 37 ks exposure obtained on 2002 February 11 (ObsID 0111100101) and was originally presented in Webb et al. (2004). The EPIC pn instrument was used in fast timing mode, while both EPIC MOS cameras were operated in full window mode. Roughly half of the observation is affected by strong background flaring, resulting in only 20 ks of usable exposure time. To generate a photon list suitable for timing and phase-resolved spectroscopy we followed the same procedure as outlined in §2.2.

Compared to the X-ray pulse profiles of PSR B1821–24 and B1937+21, the two pulse peaks of PSR J0218+4232 are appreciably broadened and their phase separation is the same, to within measurement error. In addition, there is evidence for a bridge of

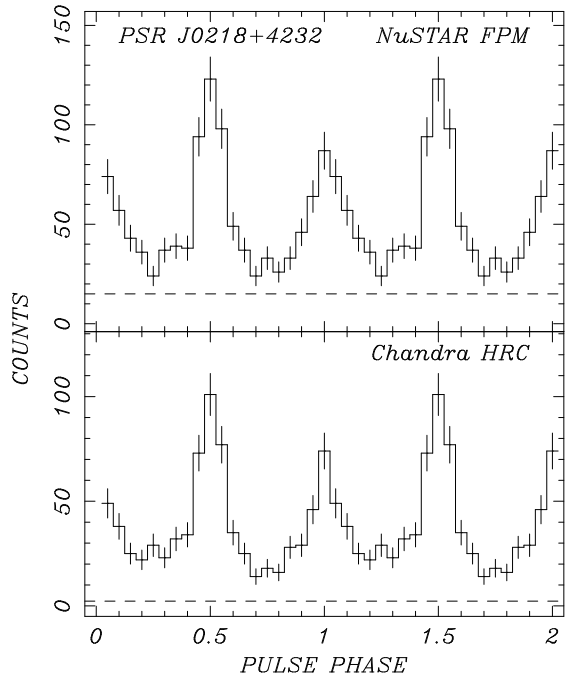


FIG. 8.— Comparison of the *NuSTAR* (top) and *Chandra* (bottom) pulse profiles of the 2.32 ms pulsar PSR J0218+4232. The *NuSTAR* 3–25 keV data are corrected for timing inaccuracies, as described in §2.2, and *Chandra* HRC-S data were obtained in fast timing mode. The background level is indicated by the dashed line. These profiles contain 20 phase bins and phase zero is arbitrarily aligned so that the main pulse peak falls on $\phi = 0.5$. Two cycles are shown for clarity.

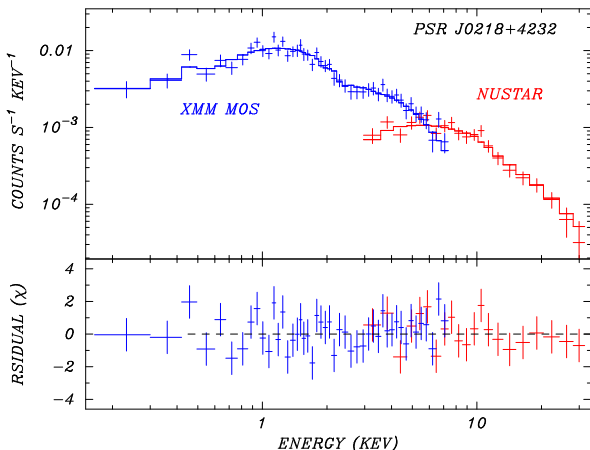


FIG. 9.— Phase-resolved *NuSTAR* spectrum of PSR J0218+4232 fitted simultaneously with the phase-averaged *XMM-Newton* MOS spectrum to an absorbed power-law model with independent normalizations. The upper panel presents the *XMM-Newton* (black) and *NuSTAR* (red) spectral data points (crosses) along with the best-fit model (solid lines) given in Table 2. The lower panel shows the fit residuals in units of sigma.

emission connecting the two peaks, with no obvious off-pulse interval. Unlike the other two MSPs, the pulsed signal for PSR J0218+4232 is not consistently detectable during a *NuSTAR* orbit with the same quality, allowing the possibility of a half-cycle phase ambiguity for some (~ 1 – 2) measurements. Nevertheless, our approach to correcting the photon arrival times is able to recover the accurate pulse profile in 0.1 ms phase bins, as shown in

Figure 8.

Mineo et al. (2000) presented evidence for energy dependence of the X-ray pulse profile of PSR J0218+4232 using *ROSAT* HRI and *BeppoSAX* data. Comparing three energy bands, 0.1–2.5 (HRI), 1.6–4, and 4–10 keV, they report that the measured flux contained in pulse (P2) increases with energy and is greater than P1 at higher energies. Furthermore, the D.C. fraction of the bridge emission decreases linearly with energy. However, a similar timing study by Webb et al. (2004) using *XMM-Newton* yielded contradictory results, where the P2 is found to be most prominent at the intermediate energy.

In the current study, we cannot address this question definitively using the *Chandra* and *NuSTAR* data as it is not possible to phase align these data in an absolute sense. However, within the limits of photon statistics, the background-subtracted HRC pulse profile, whose counts are mostly < 2 keV, is statistically identical to the background-subtracted *NuSTAR* (> 3 keV) pulse profile when aligned on the larger peaks (as shown in Figure 8). Furthermore, if we compare the (manually aligned) *NuSTAR* data in four energy bands, < 4 , 4–10, 10–20, and 20–30 keV, we find no significant evolution of the pulse profile or D.C. component with energy. We conclude that there is no convincing evidence for an energy-dependent pulse profile to date.

For a spectral analysis of PSR J0218+4232 we again extracted a *NuSTAR* spectrum for the pulsed emission only, centered on the two pulse peaks (3 + 4 of 20 phase bins). Due to a lack of a clear off-pulse interval to represent the background, we used the phase-averaged background spectrum, scaled to the on-pulse interval. We fit this *NuSTAR* spectrum simultaneously with the phase-averaged *XMM-Newton* EPIC MOS spectra and, as expected, an absorbed power-law model results in a good fit with $\Gamma = 1.10 \pm 0.09$, $N_{\text{H}} = (5.2 \pm 3) \times 10^{20} \text{ cm}^{-2}$, with $\chi^2_{\nu} = 0.88$ for 63 dof (see Figure 9). By comparing the *XMM-Newton* and *NuSTAR* best-fit fluxes, we find that the bridge emission contributes $\lesssim 35\%$ to the total in the 2–10 keV band. The lower limit allows for possible imperfections in the *NuSTAR* timing reconstruction, which might add to the bridge emission. Our spectral results are consistent with those reported in Webb et al. (2004).

5. MSP SPECTRAL ENERGY DISTRIBUTION

Using the improved constraints on the hard portion of the X-ray spectra for the three MSPs, we can re-examine the SEDs of these objects ranging from soft X-rays to GeV gamma-rays by combining our X-ray results with archival spectra in the 0.1–100 GeV band obtained with the *Fermi*-LAT. Generally, the γ -ray spectra of MSPs are well fit by a power-law model with an exponential cutoff, most typical of rotation-powered pulsars.

Johnson et al. (2013) reported on the detection of γ -ray pulsations from PSR B1821–24 at a level of 5.4σ in *Fermi*LAT data. These pulsations were misaligned from the radio and X-ray peaks, as is common among MSPs. Its γ -ray spectrum is well fit by a power-law with index $\Gamma = 1.6 \pm 0.3$ and cutoff energy $E_c = 3.3 \pm 1.5$ GeV. Similarly for PSR B1937+21, an analysis of *Fermi*-LAT data by Guillemot et al. (2012) find pulsed emission with power-law index $\Gamma = 1.43 \pm 0.87$ and a fairly low cutoff

TABLE 2
SUMMARY OF PHASE-RESOLVED SPECTROSCOPIC ANALYSIS FOR THE THREE MSPs^a

Pulsar	N_{H} (10^{21} cm $^{-2}$)	Γ	F_{X}^{b} (0.3–8 keV)	F_{X}^{b} (2–10 keV)	F_{X}^{b} (3–79 keV)	χ^2/dof
B1821–24 <i>Chandra</i> + <i>NuSTAR</i>	4.01 ± 0.04	1.28 ± 0.05	3.19 ± 0.09 [C]	3.69 ± 0.19 [N]	22.1 ± 1.5 [N]	0.91/226
B1937+21 <i>Chandra</i> + <i>XMM-Newton</i> + <i>NuSTAR</i>	17.8 ± 2.7	1.16 ± 0.11	3.01 ± 0.18 [X]	2.87 ± 0.21 [X]	18.2 ± 2.8 [N]	0.91/83
J0218+4232 <i>XMM-Newton</i> + <i>NuSTAR</i>	0.52 ± 0.3	1.10 ± 0.09	3.97 ± 0.26 [X]	3.88 ± 0.35 [X]	19.8 ± 2.3 [N]	0.88/63 Notes.

^aSimultaneous fits for the combined data sets with independent normalizations. Fits to individual data sets are presented in the text.

^bUnabsorbed flux in units of 10^{-13} erg cm $^{-2}$ s $^{-1}$, for the [C] *Chandra*, [X] *XMM-Newton*, or [N] *NuSTAR* spectral component of the composite fit.

energy of $E_c = 1.15 \pm 0.74$ GeV. PSR J0218+4232, one of the first MSPs detected with *Fermi* LAT, is characterized by a power-law index $\Gamma = 2.0 \pm 0.1$ and cutoff energy 4.6 ± 1.2 GeV (Abdo et al. 2013).

The SED of the three MSPs spanning 0.1 keV to ~ 60 GeV are shown in Figure 10. It is apparent that extrapolation of the power-law spectrum from the X-ray range to higher energies greatly overpredicts the flux in the *Fermi*-LAT band at 100 MeV and above for all three MSPs. The extrapolated X-ray spectrum is already larger than the flux in the lowest *Fermi*-LAT energy bin starting at ≈ 100 keV, ≈ 1 MeV, and ≈ 400 keV for the three MSPs, respectively. This clearly indicates that a break or smooth turnover must occur between the *NuSTAR* and the *Fermi* bands. The addition of the *NuSTAR* data, whose spectrum shows no conclusive evidence for deviation from a simple power law, requires that any spectral turnover must occur above ~ 100 keV. Due to the absence of a telescope with sufficient sensitivity between 100 keV to 100 MeV, we cannot constrain the spectrum of the three MSPs in this range. For PSR B1821–24, the presently available data with energies $\gtrsim 100$ keV from *HEXTE* and *OSSE* (from Kuiper et al. 2004) only provide upper limits on the flux that are not in conflict with the extrapolation of the X-ray power law.

The spectral energy distributions of the three MSPs are reminiscent of the high-energy emission from the Crab pulsar. In the ~ 1 –50 keV band, the Crab pulsar also shows a purely non-thermal spectrum with a power-law slope of $\Gamma \sim 2.1$, but evidence of a slight curvature. If curvature is present in the intrinsic spectrum of our MSPs, it is not discernible at a significant level with the current *NuSTAR* data. Above ~ 100 keV, the Crab pulsar spectrum turns over multiple times before increasing in the *Fermi* band (see bottom panel of Figure 10, as well as Bühler & Blandford 2014, and references therein). It is likely that the three MSPs exhibit similar spectral behavior in the 100 keV to 100 MeV range.

There exist a variety of theoretical models of pulsar electrodynamics that are used to interpret the observed high-energy magnetospheric emission from pulsars. They differ principally in the assumed location of particle acceleration and attendant emission: polar cap (e.g., Daugherty & Harding 1996), outer gap (e.g., Romani 1996), slot gap (Muslimov & Harding 2004), or beyond the light cylinder in the current sheet (see, e.g., Cerutti et al. 2016). In the context of these models where the pulsed high-energy emission originates within the magnetosphere, the observed SEDs can be understood in terms of a spectrum transitioning from a synchrotron

component at soft and hard X-ray energies to one dominated in γ -rays by either curvature radiation or synchrotron emission from the current sheet. The improved constraints on the hard X-ray spectra of the three MSPs considered here provide additional information regarding the physics of the pulsar magnetosphere. Any viable model needs to account for both the pulse shapes and the spectral energy distribution we have reported here.

6. CONCLUSIONS

We have presented detailed broadband X-ray timing and spectroscopic analyses of the magnetospheric-dominated MSPs, PSRs B1821–24, B1937+21, and J0218+4232. By making use of the sharpness of their pulses, bright enough to detect in individual telescope orbits, we are able to phase align the pulse signal between orbit gaps. By this means we are able to negate the significant drift in the *NuSTAR* clock during these gaps, likely caused by solar illumination. This allowed a phase-resolved analysis of all three pulsars.

It is important to note the limitations of this approach. The applied clock corrections are only valid during the course of an observation since the clock drift by \sim milliseconds occurs on timescales comparable to the *NuSTAR* orbit (97 minutes). In addition, the clock-correction method benefits from sharp pulsations; for fainter pulsars with broader modulations, the pulsations may not be detectable on short (orbit) intervals (see, e.g., Guillot et al. 2016 for the case of PSR J0437–4715). Imaging and temporal analysis show that the X-ray signals for PSR B1821–24 and B1937+21 are 100% pulsed, and there is no evidence for energy dependence in this energy band.

Spectra obtained with *NuSTAR* allow us to measure all three pulsars to higher energies than possible with *RXTE*, in comparable exposures, highlighting the advantage of focusing optics, which results in a substantially lower background. At these higher energies we find the same power law seen at lower energies with no conclusive evidence for a spectral break or turnover. Furthermore, the pulse profiles for all three pulsars are found to be essentially invariant with energy, from the soft to the hard X-ray bands. Combined with the GeV data from *Fermi*-LAT, we have obtained the best measurements yet of the broadband spectral shape and high-energy pulsed emission of each MSP. We find that in all cases the power-law spectrum needs to turn over somewhere above the *NuSTAR* band and below 100 MeV to be consistent with the high-energy γ -ray spectrum. This can be understood in terms of a spectrum transitioning from a dominant syn-

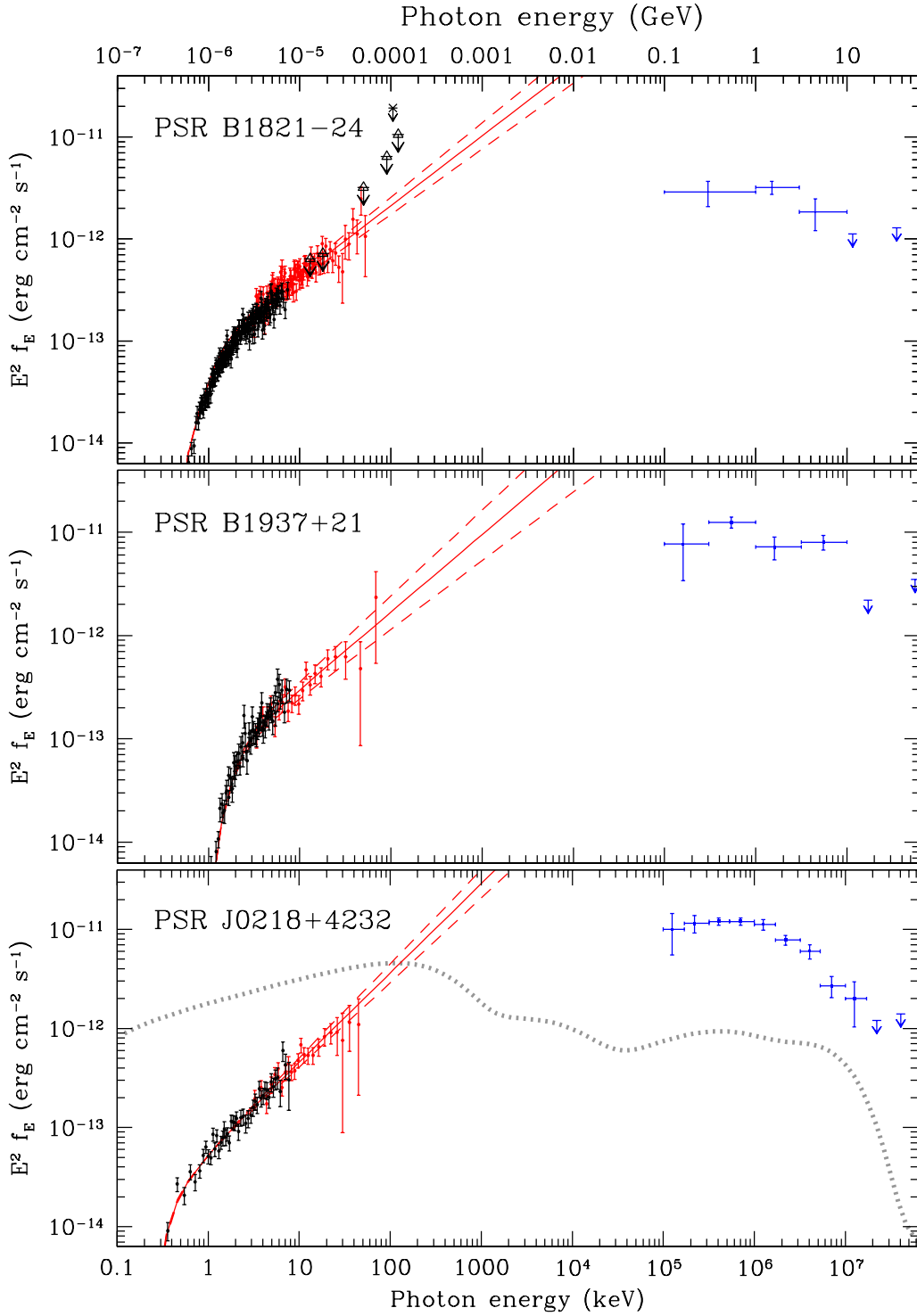


FIG. 10.— The spectral energy distribution of the three MSPs, spanning the soft X-ray to high-energy γ -ray range. The solid lines represent the respective unfolded spectra from the fits presented herein. The dashed lines are the extrapolated 90% C.L. uncertainties. The dotted line at low energies shows the unabsorbed extrapolation. The blue crosses and upper limit arrows show the *Fermi*-LAT data for photon energies ≥ 100 MeV. The open triangles and cross show the *HEXTE* and *OSSE* upper limits from Kuiper et al. (2004). top to bottom panels: PSR B1821–24, PSR B1937+21, and PSR J0218+4232. The *Fermi*-LAT spectra are from Johnson et al. (2013), Ng et al. (2014), and Abdo et al. (2013), respectively. The Crab pulsar SED (grey line) with an arbitrarily rescaled flux is shown for comparison in the bottom panel.

chrotron component in X-rays to curvature radiation or current sheet emission in γ -rays, very similar to the Crab pulsar.

We greatly appreciate discussions with M. Bachetti and C. Markwardt concerning *NuSTAR* clock timing issues, and K. Forster for the necessary assistance in

planning the PSR B1821–24 observations. We thank A. Harding for discussions regarding high-energy magnetospheric emission from pulsars. We also thank S. Ransom for supplying the radio ephemeris of PSR B1821–24. This work was supported under *NuSTAR* Cycle 1 Guest Observer Program grant NNX15AV29G awarded through Columbia University. E.V.G. thanks Josep Maria Paredes for hosting his sabbatical at the University of Barcelona Institut de Ciències del Cosmos (ICCUB) and acknowledges support through the "Programa Estatal de Foment de la Investigació Científica i Tècnica d'Excellència, Convocatòria 2014, Unitats d'Excellència *Maria de Maeztu*." The *NuSTAR* mission is a project led by the California Institute of Technology, managed by the Jet Propulsion Laboratory, and funded by the National Aeronautics and Space Administration. We thank the *NuSTAR* Operations, Software, and Calibration teams for support with the execution and analysis of

these observations. This research made use of the *NuSTAR* Data Analysis Software (NuSTARDAS) jointly developed by the ASI Science Data Center (ASDC, Italy) and the California Institute of Technology (USA). The scientific results reported in this article are based in part on data obtained from the *Chandra* Data Archive. A portion of the results presented are based on observations obtained with *XMM-Newton*, an ESA science mission with instruments and contributions directly funded by ESA member states and NASA. This research has made use of data and software provided by the High Energy Astrophysics Science Archive Research Center (HEASARC), which is a service of the Astrophysics Science Division at NASA/GSFC and the High Energy Astrophysics Division of the Smithsonian Astrophysical Observatory. We also acknowledge extensive use of the arXiv and the NASA Astrophysics Data Service (ADS).

Facilities: *NuSTAR*, *CXO*, *XMM*.

REFERENCES

- Abdo, A. A., Ackermann, M., Ajello, M. 2010, *ApJS*, 187, 460
 Abdo, A. A., Ajello, M., Allafort, A., et al. 2013, *ApJS*, 208, 17
 Arnaud, K. A. 1996, *ASPC*, 101, 17
 Backer, D. C., Kulkarni, S. R., Heiles, C., Davis, M. M., Goss, W. M. 1982, *Nature*, 300, 615
 Bahramian, A., Heinke, C. O., Tudor, V., et al. 2017, *MNRAS*, 467, 2199
 Becker, W., Swartz, D. A., Pavlov, G. G., Elsner, R. F., Grindlay, J. E., Mignani, R., Tennant, A. F., Backer, D., Pulone, L., Testa, V., & Weisskopf, M. C. 2003, *ApJ*, 594, 798
 Bégin, S., Thesis submitted to the Faculty of Physics, University of British Columbia, 2006
 Bogdanov, S., Esposito, P., Crawford, F., III, Possenti, A., McLaughlin, M. A., Freire, P. 2014, *ApJ*, 781, 6
 Bogdanov, S., Grindlay, J. E., & van den Berg, M. 2005, *ApJ*, 630, 1029
 Bogdanov, S., Grindlay, J. E., Heinke, C. O., Camilo, F., Freire, P. C. C., & Becker, W. 2006, *ApJ*, 646, 1104
 Bogdanov, S., van den Berg, M., Servillat, M., Heinke, C. O., Grindlay, J. E., Stairs, I. H., Ransom, S. M., Freire, P. C. C., Bégin, S., Becker, W. 2011, *ApJ*, 730, 81
 Bühler, R., & Blandford, R. 2014, *RPPh*, 77, 6901
 Cerutti, B., Philippov, A. A., Spitkovsky, A. 2016, *MNRAS*, 457, 2401
 Cognard, I., Shrauner, J. A., Taylor, J. H., Thorsett, S. E. 1996, *ApJ*, 457, L81
 Daugherty, J. K., Harding, A. K. 1996, *ApJ*, 458, 278
 Desvignes, G., Caballero, R. N., Lentati, L., et al. 2016, *MNRAS*, 458, 3341
 Forestell, L. M., Heinke, C. O., Cohn, H. N., Lugger, P. M., Sivakoff, G. R., Bogdanov, S., Cool, A. M., Anderson, J. 2014, *MNRAS*, 441, 757
 Guillemot, L., Johnson, T. J., Venter, C., et al. 2012, *ApJ*, 744, 33
 Guillot, S., Kaspi, V. M., Archibald, R. F., et al. 2016, *MNRAS*, 463, 2612
 Muslimov, A. G. 2002, *ApJ*, 568, 862
 Muslimov, A. G. 2005, *ApJ*, 622, 531
 Harrison, F. A., Craig, W. W., Christensen, F. E. et al. 2013, *ApJ*, 770, 103
 Jahoda, K., Swank, J. H., Giles, A. B., Stark, M. J., Strohmayer, T., Zhang, W., Morgan, E. H. 1996, *Proc. SPIE*, 2808, 59
 Johnson, T. J., Guillemot, L., Kerr, M., et al. 2013, *ApJ*, 778, 106
 Knight, H. S., Bailes, M., Manchester, R. N., Ord, S. M., Jacoby, B. A. 2006, *ApJ*, 640, 941
 Kuiper, L., Hermsen, W., Stappers, B. 2004, *AdSpR*, 33, 507
 Kuiper, L., Hermsen, W., Verbunt, F., Belloni, T. 1998, *A&A*, 336, 545
 Kuiper, L., Hermsen, W., Verbunt, F., Ord, S., Stairs, I., Lyne, A. 2002, *ApJ*, 577, 917
 Linares, M., Bahramian, A., Heinke, C., Wijnands, R., Patruno, A., Altamirano, D., Homan, J., Bogdanov, S., Pooley, D. 2014, *MNRAS*, 438, 251
 Lyne, A. G., Brinklow, A., Middleditch, J., Kulkarni, S. R., Backer, D. C. 1987, *Nature*, 328, 399
 Madsen, K. K., Harrison, F. A., Markwardt, C. B., et al. 2015, *ApJS*, 220, 8
 Manchester, R. N., Hobbs, G. B., Teoh, A. & Hobbs, M. 2005, *AJ*, 129, 1993
 Mineo, T., Cusumano, G., Kuiper, L., Hermsen, W., Massaro, E., Becker, W., Nicastro, L., Sacco, B., Verbunt, F., Lyne, A. G., Stairs, I. H., Shibata, S. 2000, *A&A*, 355, 1053
 Mori, K., Gotthelf, E. V., Dufour, F., et al. 2014, *ApJ*, 793, 88
 Muslimov, A. G., Harding, A. K. 2004, *ApJ*, 606, 1143
 Navarro, J., de Bruyn, A. G., Frail, D. A., Kulkarni, S. R., Lyne, A. G. 1995, *ApJ*, 455, L55
 Ng, C.-Y., Takata, J., Leung, G. C. K., Cheng, K. S., Philippopoulos, P. 2014, *ApJ*, 787, 167
 Nicastro, L., Cusumano, G., Löhmer, O., Kramer, M., Kuiper, L., Hermsen, W., Mineo, T., Becker, W. 2004, *A&A*, 413, 1065
 Pan, Z., Hobbs, G., Li, D., Ridolfi, A., Wang, P., Freire, P. 2016, *MNRAS*, 459, L26
 Papitto, A., Ferrigno, C., Bozzo, E., et al. 2013, *Nature*, 501, 517
 Ray, P. S., Wolff, M. T., Demorest, P., Cognard, I., Backer, D. C., Wood, K. S. 2008, *AIPC*, 983, 157
 Romani, R. W., Johnston, S. 2001, *ApJ*, 557, L93
 Romani, R. W. 1996, *ApJ*, 470, 469
 Rots, A. H., Jahoda, L., Macomb, D. J., et al. 1998, *ApJ*, 501, 749
 Rutledge, R. E., Fox, D. W., Kulkarni, S. R., Jacoby, B. A., Cognard, I., Backer, D. C., & Murray, S. S. 2004, *ApJ*, 613, 522
 Saito, Y., Kawai, N., Kamae, T., Shibata, S., Dotani, T., Kulkarni, S. R. 1997, *ApJ*, 477, L37
 Servillat, M., Heinke, C. O., Ho, W. C. G., Grindlay, J. E., Hong, J., van den Berg, M., Bogdanov, S. 2012, *MNRAS*, 423, 1556
 Takahashi, M., Shibata, S., Torii, K., Saito, Y., Kawai, N., Hirayama, M., Dotani, T., Gunji, S., Sakurai, H., Stairs, I. H., Manchester, R. N. 2001, *ApJ*, 554, 316
 Ubertini, P., Bazzano, A., Cocchi, M., Natalucci, L., Heise, J., Muller, J. M., in't Zand, J. J. M. 1999, *ApJ*, 514, L27
 Verner, D. A., Ferland, G. J., Korista, K. T., Yakovlev, D. G. 1996, *ApJ*, 465, 487
 Verbunt, F., Kuiper, L., Belloni, T., Johnston, H. M., de Bruyn, A. G., Hermsen, W., van der Klis, M. 1996, *A&A*, 311, L9
 Webb, N. A., Olive, J. -F., & Barret, D. 2004, *A&A*, 417, 181
 Wilms, J., Allen, A., & McCray, R. 2000, *ApJ*, 542, 914
 Zavlin, V. E. 2006, *ApJ*, 638, 951
 Zavlin, V. E. 2007, *Ap&SS*, 308, 297